

## ASTROMETRIC PERTURBATIONS IN SUBSTRUCTURE LENSING

JACQUELINE CHEN<sup>1</sup>, EDUARDO ROZO<sup>2</sup>, NEAL DALAL<sup>3</sup>, & JAMES E. TAYLOR<sup>4</sup>

*Draft version July 2, 2018*

### ABSTRACT

In recent years, gravitational lensing has been used as a means to detect substructure in galaxy-sized halos, via anomalous flux ratios in quadruply-imaged lenses. In addition to causing anomalous flux ratios, substructure may also perturb the positions of lensed images at observable levels. In this paper, we numerically investigate the scale of such astrometric perturbations using realistic models of substructure distributions. Substructure distributions that project clumps near the Einstein radius of the lens result in perturbations that are the least degenerate with the best-fit smooth macromodel, with residuals at the milliarcsecond scale. Degeneracies between the center of the lens potential and astrometric perturbations suggest that milliarcsecond constraints on the center of the lensing potential boost the observed astrometric perturbations by an order of magnitude compared to leaving the center of the lens as a free parameter. In addition, we discuss methods of substructure detection via astrometric perturbations that avoid full lens modeling in favor of local image observables and also discuss modeling of systems with luminous satellites to constrain the masses of those satellites.

*Subject headings:* cosmology: theory – dark matter – gravitational lensing

### 1. INTRODUCTION

The cold dark matter (CDM) paradigm predicts that the dark matter (DM) halos hosting most galaxies contain a large number of low-mass, compact subhalos within their virialized regions. These subclumps, collectively referred to as substructure, may or may not contain luminous stellar tracers. Since the observed number of dwarf galaxy satellites in the Local Group falls short of the expected number of subhalos by more than an order of magnitude (Klypin et al. 1999b; Moore et al. 1999), then either the CDM model is incorrect or dwarf galaxies are biased tracers of DM in galaxy-scale halos (e.g., Spergel & Steinhardt 2000; Hannestad & Scherrer 2000; Hu et al. 2000; Bullock et al. 2000; Benson et al. 2002; Somerville 2002; Stoehr 2002; Nagai & Kravtsov 2005). If the CDM paradigm is correct, then the paucity of optical counterparts of substructures leaves us with few avenues for detecting and investigating DM substructure.

One possibility for studying dark substructure around local galaxies is through its perturbative effect on kinematically cold systems like tidal streams (e.g., Mayer et al. 2002) or galactic disks (e.g., Toth & Ostriker 1992; Benson et al. 2004). These tests probe only the closest and most massive substructures, and are only applicable in very nearby galaxies. As a result, this method provides little information to address fundamental questions such as the amplitude of the matter power spectrum on subgalactic scales or the detailed

properties of dark matter itself.

Another promising method of study is through the gravitational lensing effects of substructure, referred to as substructure lensing. Much of the previous work in this field has focused on the effects of substructure on image magnifications and fluxes (Mao & Schneider 1998; Metcalf & Madau 2001; Dalal & Kochanek 2002; Kochanek & Dalal 2004; Rozo et al. 2006) or on time delays (Morgan et al. 2006). However, substructure can perturb the deflection angle,  $\alpha$ , of lensed images as well. Image positions in lensed systems may not be subject to the same foregrounds – such as dust absorption – as flux anomalies. Further, since the astrometric perturbation,  $\delta\alpha$ , is a steeper function of subhalo mass than flux perturbations, it may provide a qualitatively distinct probe of substructure properties.

A study of astrometric perturbations is particularly timely given the possibility of submilliarcsecond resolution observations of strong lenses. For example, Biggs et al. (2004) have presented observations of a four image jet source system, CLASS B0128+437, in which milliarcsecond astrometric perturbations may have been detected. Previous studies of astrometric perturbations by substructures have come to conflicting conclusions about their overall size and probability. Metcalf & Madau (2001) use lensing simulations of random realizations of substructure in regions near images to suggest that in order to change image positions by a few tens of milliarcseconds (mas), there must be subclumps with masses  $\gtrsim 10^8 M_\odot$  in Milky Way sized halos that are well aligned with the images they perturb. This alignment is likely to be rare in CDM, although the probability would increase in systems where the source is elongated in a jet (Metcalf 2002). On the other hand, Chiba (2002) tests the size of astrometric perturbations in B1422+231 with a model of CDM subhalos as point masses and finds deflections of 10 to 20 mas, using subclumps with masses greater than  $\sim 2 \times 10^8 h^{-1} M_\odot$ . Additional studies of astrometric perturbations by single

<sup>1</sup> Argelander-Institut für Astronomie, Universität Bonn, Auf dem Hügel 71, D-53121 Bonn; jchen@astro.uni-bonn.de

<sup>2</sup> CCAPP Postdoctoral Fellow, Department of Physics, The Ohio State University, 1040 Physics Research Building 191 West Woodruff Avenue Columbus, Ohio 43210-1117; erozo@mps.ohio-state.edu

<sup>3</sup> Canadian Institute for Theoretical Astrophysics, University of Toronto, 60 St. George St., Toronto, Ontario, Canada M5S 3H8; neal@cita.utoronto.edu

<sup>4</sup> Department of Physics and Astronomy, University of Waterloo 200 University Avenue West, Waterloo, Ontario, Canada N2L3G1; taylor@uwaterloo.ca

perturbers have focused on the detection of substructure via distortion of a finite source (Inoue & Chiba 2003, 2005a,b). In addition, Pen & Mao (2005) studied the effect of multiple lens planes on the rotation of lensed images.

In this paper, we estimate the amplitude of astrometric perturbations produced by substructures using realistic substructure models and test the feasibility of observing such perturbations by comparison with the image positions given by a best-fit lens macromodel. While Metcalf & Madau (2001) suggest that single clumps need to be well aligned with the images in order to produce observable perturbations, measurable effects may be possible in more general scenarios, given the collective effects of entire substructure distributions. In addition, the kinds of perturbations in these scenarios may be different. For example, while the scenario of a nearby subhalo that perturbs only a single image ensures that degeneracies with best-fit smooth macromodels are small, large numbers of more distant substructure may affect multiple images and exhibit large degeneracies with the macromodel. In addition to using detailed lens modeling, we discuss model-independent methods for identifying substructures, proposing a method using systems with multiply imaged jets.

Substructure lensing may also be used for comparisons between luminous satellites and dark subhalos. For example, we can address one of the open questions regarding CDM substructure: why are some subhalos dark and some luminous? There have been many proposed mechanisms to explain which subhalos have stars and which do not. One possibility is that the efficiency of star formation diminishes with decreasing halo mass, perhaps due to photoionization squelching (Bullock et al. 2001). Another suggestion has been that luminous galaxies form only in the highest mass halos ( $M > 10^9 M_\odot$ ), and over time tidal stripping reduces subhalo masses to the low values ( $M \sim 10^8 M_\odot$ ) inferred for the smallest local dwarfs (Kravtsov et al. 2004b). Yet another possibility is that the low masses inferred for local dwarfs are in fact mistaken, and instead are much larger,  $M \gtrsim 10^9 M_\odot$  (Stoehr et al. 2002, 2003). Kazantzidis et al. (2004) find that subhalos do not experience the significant mass redistribution in their centers required to embed satellites in massive subhalos, and studies stellar kinematics in the dwarfs also dispute the existence of massive subhalos (e.g., Wilkinson et al. 2004). Here, we propose directly measuring the masses associated with luminous satellites projected near lensed images, the results of which would directly test the Stoehr et al. (2002) hypothesis.

The layout of the paper is as follows. We begin by describing the host halo and substructure models we will be employing in our analysis in §2. The statistical properties of the astrometric perturbations in our models are presented in §3, and their degeneracy with macro-lens model parameters is discussed in §4. We discuss model-independent, astrometric signatures of substructure lensing in §5. Finally, the effect of luminous substructures on astrometric perturbations and lens modeling is discussed in §6, and we present a summary of our results and conclusions in section §7.

## 2. NUMERICAL ESTIMATES

In this section we present the host halo and substructure models we used to analyze astrometric perturbations and describe our methods of creating artificial lens systems with substructure, finding the image positions in such systems, and fitting for the best-fit smooth model.

### 2.1. Halo Model

We begin by specifying the macromodel parameters of the lens system – using typical lens parameters – and the background cosmology used to generate artificial lenses. In particular, we choose a lens redshift of  $z_l = 0.5$ , a source redshift of  $z_s = 2.0$ , and a flat  $\Lambda$ CDM cosmology with  $\Omega_m = 0.3$ ,  $\Omega_\Lambda = 0.7$ , and  $h = 0.7$ . The halo of the lensing galaxy is modeled as a singular isothermal ellipsoid (SIE), the projected density profile of which is given by

$$\kappa(\xi) = \frac{b}{2\xi}, \quad (1)$$

where  $\xi$  is the projected radius,  $\xi^2 = x^2 + y^2/q^2$  and  $q = 0.9$  is our fiducial value for the lens's axis ratio. The particular values for the ellipticity and shear do not appear to be significant to the results of this paper. The length scale  $b$  corresponds to the Einstein radius of the lens for circularly symmetric profiles ( $q = 1$ ). We take as our fiducial value  $b = 1.05''$ , corresponding to the Einstein radius of a singular isothermal sphere of mass  $M = 10^{13} M_\odot$  in our chosen cosmology and source and lens redshifts. Finally, we assume there is an external tidal shear of  $\gamma = 0.16$  aligned with the major axis of the halo ( $\theta_\gamma = 0$ ). Our particular choice  $\gamma = 0.16$  corresponds to the best-fit value for the external shear obtained by Bradač et al. (2002) for the lens system B1422+231, a system known to exhibit anomalous flux ratios.

### 2.2. Substructure Models

We employ four different subhalo catalogs to populate our fiducial halo with substructures. The catalogs describe the three-dimensional position in the parent halo and the density profile of each subhalo. In order to use these catalogs in our halo model, the substructure positions and density profiles must be projected along an axis. The density profiles are projected by parameterizing the spherical density profiles in three dimensions, then using an approximate formula for the profile in two dimensions. The following section describes the substructure models in detail.

For two of these models, we use substructure catalogs from a DM cluster simulation with  $\Omega_m = 0.3$ ,  $\Omega_\Lambda = 0.7$ ,  $h = 0.7$ , and  $\sigma_8 = 0.9$ . The adaptive-refinement-tree (ART) code is used to run the simulation (Kravtsov et al. 1997; Kravtsov 1999), using a  $256^3$  uniform root grid covering the computational box of  $80h^{-1}$  Mpc and resimulating a cluster in the box with more particles and higher spatial resolution (Tasitsiomi et al. 2004). For this higher resolution simulation, the effective mass resolution is  $m_p = 3.95 \times 10^7 h^{-1} M_\odot$  and the smallest cell size reached is  $0.6h^{-1}$  comoving kiloparsecs. Details of the simulations can be found in Nagai & Kravtsov (2005). A variant of the Bound Density Maxima halo finding algorithm (Klypin et al. 1999a) is used to identify subhalos. Details of the algorithm used to find subhalos can be found in Kravtsov et al. (2004a).

We draw two different subhalo catalogs from the cluster simulation, one at  $z=0.5$ , as the cluster is undergoing a major merger, and another at  $z=0$ . The mass of the parent halo itself is scaled down to  $10^{13} M_{\odot}$  and all sub-clumps are scaled accordingly<sup>5</sup>. Finally, clumps within the virial radius with mass  $M \geq 10^8 M_{\odot}$  ( $M/M_{vir} \geq 10^{-5}$ ) are chosen. These clumps correspond to  $N_P \geq 80$ . Nagai & Kravtsov (2005) show that the mass function of the high resolution simulation converges with that of a lower resolution simulation for  $N_P \geq 80$ . We fit the clumps with a Moore profile (Moore et al. 1999),

$$\rho(r) = \frac{\rho_s}{(r/r_s)^{1.5}(1+(r/r_s)^{1.5})} \quad (2)$$

truncated at a radius  $r_t$  using a Levenberg-Marquardt minimization technique. The resulting overall mass fraction in substructure is 10% at  $z=0.5$  and 13% at  $z=0$ . The left-hand panels of Figures 1 and 2 show the number density profile and cumulative mass function for both redshift samples.

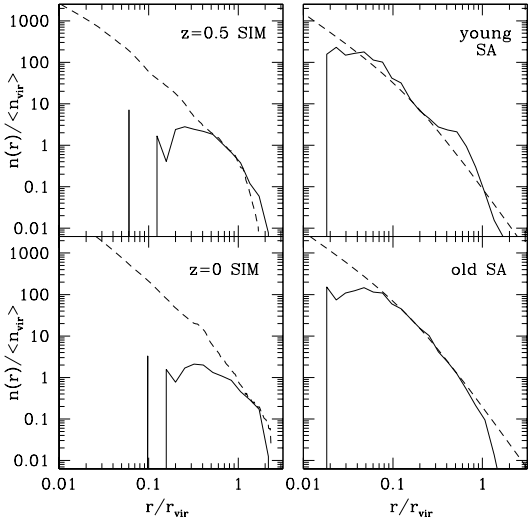


FIG. 1.— *Left:* The number density profile of subhalos from numerical models normalized to the number density within the three dimensional virial radius,  $n(r)/\langle n_{vir} \rangle$ , for  $z=0.5$  (top) and  $z=0$  (bottom). The dashed line shows the dark matter profile normalized to the virial overdensity. *Right:* The number density profile of subhalos from semi-analytic models normalized to the number density within the virial radius,  $n(r)/\langle n_{vir} \rangle$ , for a young halo (top) and an old halo (bottom), using all clumps with masses greater than  $M = 10^8 M_{\odot}$ . The dashed line shows a Moore profile with concentration of 6.4, normalized to the scale radius.

Compared to galactic halo, the scaled cluster simulation may have a greater number of substructures (Zentner et al. 2005a) – although in our substructure catalogs, the substructure mass fraction does not seem significantly larger than expected at 10-20%. In addition, we may expect that the concentration of the subclumps in the cluster simulation may be smaller than in a comparable galactic halo; the issue of subhalo concentrations is further discussed in Section §4.4.

<sup>5</sup> Although the two catalogs are drawn from different epochs, we use both for ad hoc substructure distributions in the lens at the lens redshift and, therefore, fix the masses and virial radii to the same values.

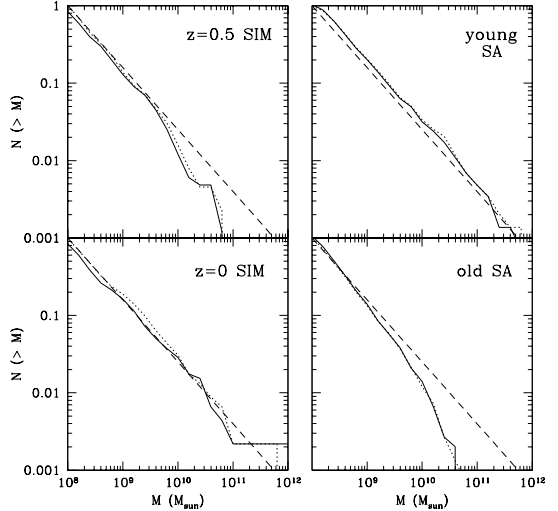


FIG. 2.— *Left:* The cumulative mass function of subhalos from numerical models enclosed within the virial radius, for subhalos at  $z=0.5$  (top) and  $z=0$  (bottom). *Right:* The cumulative mass function of subhalos from semi-analytic models enclosed within the virial radius for subhalos for a young halo (top) and an old halo (bottom). In all panels, the mass function from the three dimensional mass profile is a dotted line, the mass function derived from the parameterization of the subhalos using Eqn. 4 is a solid line and the normalized  $n \sim m^{-1.8}$  mass function is a dashed line.

The radial distribution of subhalos may be weakly dependent upon the mass scale of the parent halo (Gao et al. 2004; Diemand et al. 2004), with a cluster-scale simulation with fewer subclumps in the center of the halo than a galaxy-scale simulation. In addition, simulations may suffer from overmerging in the center of halos, reducing the number of subclumps in the inner portions of the halo (Moore et al. 1996; Klypin et al. 1999a). This effect may be particularly important in lensing studies, where substructure close to the projected center of the system produces the strongest perturbations. To get an independent estimate of how much substructure might survive in the inner parts of galaxy halos, we consider substructure distributions in two halos constructed using the semi-analytic model described in Taylor & Babul (2001, 2004); these models – like our simulation models – do not include a galaxy component, but contain much more substructure in the central regions of the cluster (Taylor & Babul 2005), thus likely providing an upper limit to the amount of substructure in CDM halos.

The semi-analytic models assume spherical symmetry in the input orbits and the potential, and all clumps are parameterized by a Moore profile, truncated at  $r_t$  and decreased in density by a fraction  $f_t$  as in Hayashi et al. (2003) (equation 8):

$$\rho(r) = \frac{f_t}{1 + (r/r_t)^3} \frac{\rho_s}{((r/r_s)^{1.5})(1 + (r/r_s)^{1.5})}. \quad (3)$$

Kazantzidis et al. (2004) suggests that the Hayashi et al. (2003) relation may reflect lowered concentrations in the subhalos simulation due to nonequilibrium initial conditions combined with numerical resolution rather than tidal shocks; the issue of subhalo concentrations is further discussed in Section §4.4.

The two semi-analytical substructure catalogs we choose correspond to a dynamically old and a dynam-

ically young parent halo at  $z=0$ . The old halo has accreted 50% of the parent halo's mass by  $z=3.2$  and 90% by  $z=0.67$ . The corresponding redshifts for the young halo are 0.54 and 0.04. Finally, the old halo has a substructure mass fraction of 10%, while the young halo has a mass fraction of 21%. We scale the host halo mass – a galactic halo of  $1.6 \times 10^{12} M_{\odot}$  – to  $10^{13} M_{\odot}$  and scale all the substructures accordingly, keeping only those substructures with rescaled masses larger than  $10^8 M_{\odot}$ . The right-hand panels of Figures 1 and 2 show the resulting number density profile and cumulative mass function for both samples.

In comparison to the simulation profiles, the semi-analytic catalogs have many more clumps in the center of the halo, while the number density profiles of all the substructure models track the host halo dark matter profile at large radii. In addition, the mass functions of all the substructure models are similar,  $n \sim m^{-1.8}$ , as expected from the results of high resolution numerical simulations (Ghigna et al. 2000). In both the simulation substructure models and the semi-analytic models, one of the distributions follows  $n \sim m^{-1.8}$  to masses greater than 1% of the halo mass, while the other distribution falls off and has fewer large-mass clumps. We shall see that the presence or absence of large mass clumps can have important consequences on the distribution of position perturbations.

In addition to specifying the general properties of the host halo and its substructure population, lensing calculations require we specify a line-of-sight projection axis. We have chosen to project all halos along the major axis of the host halo. This choice for line-of-sight projection is motivated by the fact that it results in the most compact, and therefore most effective, lenses. Consequently, one might expect most observed strong lens systems to be projected along this axis. Moreover, this projection leads to the largest substructure densities in the central part of the halo, which should maximize the impact substructures have on the lensed images (Zentner et al. 2005b).

As expected, the projected substructure distributions obtained from the simulation catalogs have fewer clumps in the central regions of the halo than the projected semi-analytic models. For instance, within  $2''$  of the center of the lens, the  $z = 0.5$  simulation projection has no clumps and the  $z = 0$  simulation has 1 clump of mass  $3.8 \times 10^8 M_{\odot}$ , or  $\sim 0.5\%$  of the halo mass *that is enclosed within the Einstein radius*. On the other hand, both semi-analytic models have 7 clumps within this projected radius, with total masses of  $6.5 \times 10^9 M_{\odot}$  and  $7.1 \times 10^9 M_{\odot}$  for the dynamically old and dynamically young catalogs respectively, or  $\sim 5 - 10\%$  of the halo mass *that is enclosed within the Einstein radius*. For future reference, we note that the  $z = 0$  simulation model has the largest subclump of all the models,  $\sim 7\%$  of the halo mass, and this subclump is projected far from the Einstein radius of the host halo.

Rather than modeling the two dimensional mass profile of each individual substructure as a projected Moore or Hayashi profile, we use the approximation,

$$\kappa(x) = \frac{3.5\kappa_s}{x^{1/2} + x^2}, \quad (4)$$

where  $\kappa_s = 2\rho_s r_s$  for projected Moore profiles and  $\kappa_s = 2f_t \rho_s r_s$  for the Hayashi profile, and  $x = 2.4R/r_s$  where  $R$  is the projected radius. Our choice of profile is numerically motivated in that the deflection angle associated with our chosen profile has a simple closed form expression, whereas the projected Moore profile does not. We show the mass functions of the substructure distributions using this approximation in Fig. 2 (solid lines). Note our approximation does not appreciably bias the substructure mass functions.

### 2.3. Generating and Modeling Artificial Lenses

Our host halo and substructure models are used to generate artificial lenses as follows. First, the image positions of a given point source are obtained by finding all roots of the lens equation using a Newton-Raphson root finder with a gridded set of initial guesses. Once the image positions of a source are obtained, we fit the resulting lens system with a lens model that parameterizes the smooth components of the lens only. We then compare the true image position with that obtained in the absence of substructures and with that predicted by the best-fit model for each image in the lens. We repeat this experiment to statistically sample the source plane in order to obtain distributions for the astrometric perturbations generated by the dark matter substructures.

The results of such a statistical comparison obviously depend on the how the source plane is sampled. While naively one might expect uniform source plane sampling to be adequate, observed lens samples suffer from magnification bias (brighter systems are more likely to be observed than dimmer systems) and consequently magnification weighted sampling is the most appropriate choice. Keeton & Zabludoff (2004) show that for sources with a power law luminosity function,  $dN/dS \propto S^{-\nu}$  with  $\nu = 2$ , magnification weighting in the source plane is equivalent to uniform sampling of the *image* plane. The importance of this result rests on the fact that uniform image plane sampling is easy to implement and the fortuitous fact that the observed quasar luminosity function in the largest lens surveys is roughly a power law with an index,  $\nu \approx 2$ . Consequently, we have opted for distributing sources along the source plane in accordance with uniform image plane weighting in order to provide a closer match to observations.

Best-fit models to artificial lenses are obtained by  $\chi^2$  minimization with a downhill simplex algorithm. If convergence is not achieved within a prescribed number of steps, the original input parameters (the macromodel parameters) are perturbed and the modeling is repeated until convergence is achieved. The  $\chi^2$  minimization puts priors on parity agreement and excessively magnified images during modeling. We eliminate extremely dim images,  $\mu < 0.01$ , and systems with excessively magnified images,  $\mu > 50$ . Finally, an appropriate best-fit model may not be found if the simplex travels to an area of parameter space that produces a number of modeled images that is different from the observed number of images.

The smooth models used in the minimization are comprised of an SIE mass distribution along with an external shear component. The model parameters are the Einstein radius  $b$ , the projected axis ratio  $q$ , the external shear  $\gamma$ , the orientation of the shear  $\theta_{\gamma}$ , the orientation of the ellipticity  $\theta_q$ , the center of the potential  $x_{\text{origin}}$  and

$y_{\text{origin}}$ , and the coordinates of the source position  $x_{\text{source}}$  and  $y_{\text{source}}$ .

Notice that lens systems with a single source position have nine parameters to be fit whereas there are only eight observables in quadruply imaged systems. To make the system overconstrained, we artificially hold the origin (i.e., the position of the SIE) fixed at  $(x, y) = (0, 0)$ , thereby reducing the number of free parameters to seven. Observationally, this can be accomplished by fixing the center of the mass distribution to the observed position of the lensing galaxy. Recent work by Yoo et al. (2005) suggest that the position of the lensing galaxy is an appropriate approximation of the center of the lensing potential. For lens systems with more than a single source position (i.e., jet sources), quadruply imaged systems will always be overconstrained without reducing the number of parameters. Note that in all sections, we restrict ourselves to four image lenses.

### 3. INTRINSIC ASTROMETRIC PERTURBATIONS

In this section we investigate the intrinsic perturbations generated by substructure: the position difference between images generated by a parent halo alone and images generated by a parent halo with substructure. While observationally we are interested in the residuals relative to the best-fit model, comparisons to the intrinsic perturbations allow us to determine to what extent perturbations by substructure are degenerate with changes in the macromodel parameters of the best-fit lens.

Our initial expectations for intrinsic perturbations are colored by our understanding of single perturbers. Consider the case of adding a single perturber to a smooth macromodel; it is clear that the astrometric perturbation will scale with the the size and radial position of the perturber, so that larger and more centrally located subclumps produce larger perturbations. In the case of substructure distributions, however, it is unclear if the most massive/most centrally located substructures will dominate the astrometric perturbations. For instance, the steepness of the mass function means that there are many more small perturbers than large, so if the former act cooperatively they could in principle generate a large perturbation. Conversely, since oppositely positioned perturbers generate equal and opposite perturbations, the net effect of a large number of substructures may cancel out ensuring that rare, massive substructures dominate the position perturbation of the images.

Figure 3 shows the intrinsic perturbation distribution for each of the fiducial substructure models considered; each system is quadruply-imaged and the residual for each image position is calculated. We note here that in this figure – as in all of our subsequent figures involving histograms of residuals – shows the results in a logarithmic scale. Testing the entire subclump distributions, we find that the residual distributions all have very large peak perturbations,  $\gtrsim 10$  mas. Interestingly, our simulation-derived substructure models result in residuals that are comparable to or larger than those of the semi-analytic models, demonstrating that the intrinsic astrometric perturbations are not necessarily dominated by nearby clumps. In addition, since the simulation models have extremely few or no substructures near the Einstein radius of the lens and therefore the perturbers must be located further away, we can infer that position per-

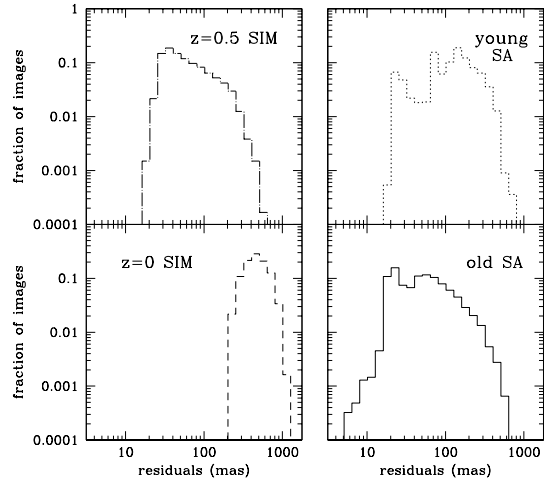


FIG. 3.— Histograms of the residuals between observed images in milliarcseconds for systems with substructure and without substructure for quadruply-imaged single point source systems. The panels show the  $z = 0.5$  simulation distribution (top-left) dynamically young semi-analytic substructure distribution (top-right), the dynamically old semi-analytic distribution (bottom-right), and the  $z = 0$  simulation distribution (bottom-left).

turbations of different images in any lens configuration may be strongly correlated. A final interesting quality of our residual is that the two simulations with the largest peak residuals are also the two models that have very massive substructures. This suggests that rare, massive clumps may cause larger perturbations than the more abundant smaller clumps. However, even in the models where no such massive substructures are present, the astrometric perturbations of the images is still considerable.

### 4. MODELED RESIDUALS

In general, the intrinsic perturbations just discussed are at least partly degenerate with macromodel parameters. For instance, substructure can change the macromodel by adding to the total projected mass distribution and increasing the Einstein radius,  $b$ ; by changing the ellipticity or orientation of the macromodel; and by adding external shear to the potential. For example, the perturbations from a single subclump placed far from the lens are degenerate with an external shear. We expect then that the modeled residuals, residuals between the observed image positions and the image positions predicted by the best fit smooth macro-model to the lens, will be smaller than the intrinsic residuals discussed above.

We test the extent to which the intrinsic perturbations can be accommodated with the macromodel and whether the remaining perturbations (i.e., the perturbations relative to the best-fit model) are large enough to be detectable. We consider only quadruply-imaged systems and test two possible lens modeling scenarios: (1) a single point source system modeled with the 7 parameters mentioned earlier ( $b, q, \theta_q, \gamma, \theta_\gamma, \vec{r}_{\text{source}}$ , with the center of the potential fixed) and (2) a jet source, approximated by two source positions separated by 10 mas and modeled by 11 parameters, including the center of the potential and two source positions. In jet source cases, we refer to each pair of images produced by the source positions together as an image of the jet, and refer to the image of each individual subsource as a subimage.

#### 4.1. Automated Lens Fitting

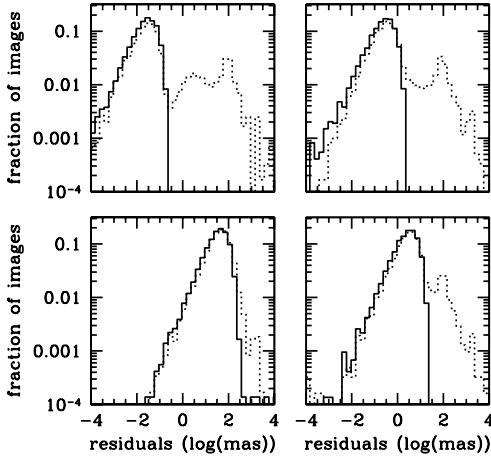


FIG. 4.— Histograms of the residuals between modeled and observed images in milliarcseconds for single point source systems using 7 fitted parameters and fixing the center of the lens potential to  $(x,y)=(0,0)$ . Only four image systems are plotted. In each panel the solid line indicates images with Gaussian errors and no substructure, while the dotted line is the same, where the initial guess for the Einstein radius is underestimated by 10%. Clockwise from the top-left panel, Gaussian errors with a standard deviation of 0.1, 1, 10, and 100 mas are shown. We can see that a tail of large residuals is an artifact of our fitting procedure, though the peak perturbation scale is robustly determined. Consequently, in all future plots of residual distributions we focus only on the scale at which the distribution peaks. The tail of high residuals comprises about 10% of the total number of sources considered for each model ( $\approx 10000$ ).

Before we move on to results, a discussion of one of the difficulties in the automated lens fitting procedure is required. The lens fitting is done through a simple downhill simplex algorithm. If our initial guess for the best-fit model is not in the same  $\chi^2$  valley as the true best-fit model, our resulting formal best-fit model can be quite far from the true best-fit smooth macromodel. We illustrate this point in Figure 4. For this figure, we generated lenses using the smooth host halo mass distribution only (no substructure), and then added Gaussian perturbations of 0.1, 1, 10, and 100 mas to the image positions in successive panels. The resulting lenses were then fit starting from two different initial guesses for the best fit model. For the first, shown in Figure 4 as a solid line, we used the original mass distribution used to generate the lens in the first place (i.e., the "correct" smooth mass model). For the second, shown with the dotted line in Figure 4, we simply lowered our initial best guess for the Einstein radius by 10%. In all cases, only four image systems are used and the residual from each image is calculated. As is evident from Figure 4, in the first case the lens is always fit correctly, and the residual distributions are sharply cut around the scale of the deviation, exactly as we would expect. On the other hand, for the second case we find that there is a large, unphysical tail of high residuals. This tail was found in all of our substructure runs, and accounts for about  $\approx 10\%$  of the systems fit. This relation is true for Gaussian perturbations regardless of the size of the perturbations.

In the remaining sections of our work, we ignore this

tail as an artifact of our lens fitting algorithm. More importantly, the *peak* of the residual distribution is correctly recovered by our algorithm, and the location of the peak in our substructure runs has physical significance.

#### 4.2. Substructure Degeneracies with Macromodels

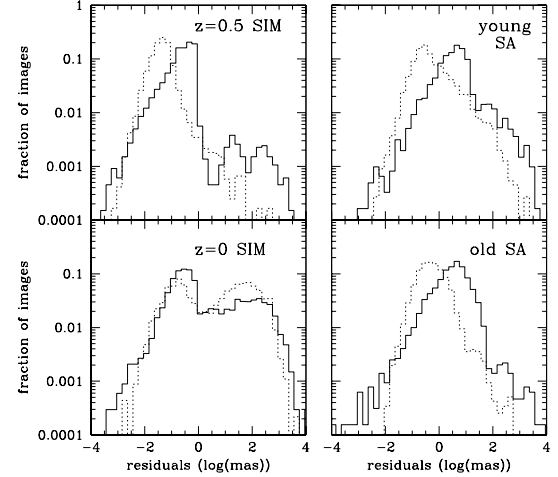


FIG. 5.— Histograms of the residuals between modeled and observed images in milliarcseconds for single point source systems using 7 fitted parameters and fixing the center of the lens potential to  $(x,y)=(0,0)$  (solid) and for jet source systems using 11 fitted parameters (dotted). Only four image systems are plotted. The panels show the  $z = 0.5$  simulation distribution (*top-left*) dynamically young semi-analytic substructure distribution (*top-right*), the dynamically old semi-analytic distribution (*bottom-right*), and the  $z = 0$  simulation distribution (*bottom-left*).

We present the residual distribution for the single source and jet source scenarios using realistic substructure distributions in Fig. 5. Here, the modeled residuals are small and, for the most part, significantly smaller than the intrinsic residuals discussed in the previous section, with the peak perturbations occurring between .1 mas and 10 mas. The decrease in the size of the peak perturbations with respect to the intrinsic perturbations reflects the fact that there is significant degeneracy between the subclumps and the macromodel.

Comparing the different substructure distributions, we see that for the single source case, the semi-analytic substructure models produce larger perturbations than the simulation substructure models. This difference is evidence for the importance of having substructures within the neighborhood of the Einstein radius of the lens in order for the system to exhibit observable astrometric perturbations. It is also worth noting that the  $z = 0$  simulation substructure model had the largest intrinsic position residuals and has the largest fraction of poor modeled fits – demonstrating that a massive but distant clump changes the macromodel enough to be more difficult to find a best-fit model. The acceptable modeled residuals, however, are comparable to that of the  $z = 0.5$  simulations, showing that those perturbations induced by a massive but distant clump are degenerate with an external shear.

In addition to substructure model differences, there are significant differences between single point source systems, where we hold the center of the lens potential fixed,

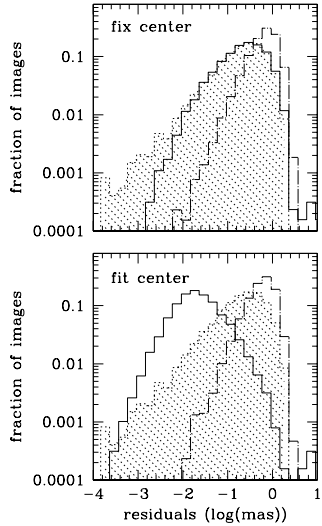


FIG. 6.— Histograms of the residuals between modeled and observed images in milliarcseconds for images with Gaussian errors with a standard deviation of 1 mas and no substructure. For jet sources, each subimage is perturbed separately in the dot-dashed line but both subimages are perturbed by the same amount in solid line. In both panels, the shaded, dotted histogram shows the distribution when employing single point source systems, with the center of the lensing potential fixed. *Top:* The center of the lensing potential is held fixed for the jet source systems. *Bottom:* The center of the lensing potential is fit for the jet source systems.

and jet source systems, in which the center is allowed to float. When jet sources are used, modeled residuals are *smaller* than the corresponding residuals in the single source case. This result is contrary to our naive expectations. One could imagine taking each set of four subimages, and fitting each individually with a mass model. Since the best-fit models for each set of four subimages will in general differ, a single mass model for all eight images should result in larger residuals. The resolution to this problem becomes apparent when we realize that in fitting jet sources we have allowed the center of the potential to float, so the added freedom could result in a better fit. Now, in practice, we find that this added freedom does result in better fits, but this didn't have to be the case, i.e., substructure position perturbations did not have to be degenerate with a change in the position of the lens's center *a priori*.

We illustrate this point in Figure 6. The figure is produced by adding 1 mas Gaussian errors to images for both single point source systems and jet source systems as lensed in the absence of substructures (i.e., we use only the smooth halo component to generate the artificial lenses). In addition, we test two methods of adding the Gaussian errors to the jet source systems; in one, each subimage is perturbed independently of the other, while, in the other, each image is perturbed separately, but the two subimages of the each lensed image are perturbed in the same way. We then proceed to fit the artificial lenses. As before, single point source systems are modeled by holding the center of the potential fixed. Jet source systems, on the other hand, are modeled both with the center of the potential fixed and with the center of the potential allowed to float. For the former case (top panel), we find that, just as we would expect, the single source case (filled, dotted histogram) results in smaller

residuals than the jet source case (dot-dashed line) when each subimage is perturbed independently. When each subimage pair is perturbed in the same way, the resulting histogram (solid line) is essentially identical to that of the single point source case, again in agreement with our expectations. Turning now to the bottom panel of Figure 6 in which the center of the potential is allowed to float, we find that this added freedom leaves the residual distribution of the jet source unchanged when each subimage is perturbed independently. When each member of a subimage pair is perturbed in the same manner, however, the distribution of residuals changes dramatically, and in particular the peak residual is an order of magnitude lower than what we found when the center of the potential was held fixed. Thus, our observed residual distribution from the substructure lenses indicates that the position perturbations generated by substructures are coherent on scales at least as large as the assumed extent of our jet source.

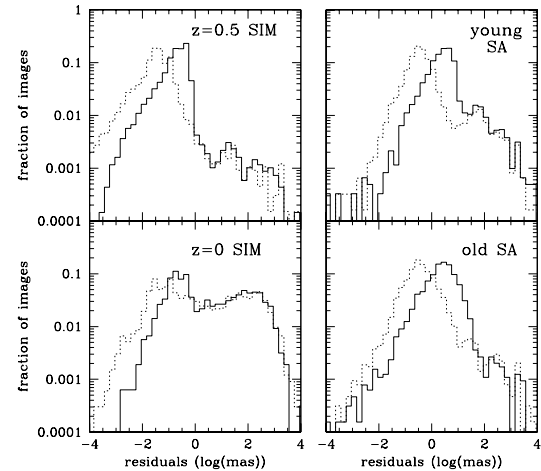


FIG. 7.— Histograms of the residuals between modeled and observed images in milliarcseconds for single point source systems using 7 fitted parameters and Gaussian priors on the center of the lens potential of 5 mas (dotted) and 1 mas (solid). Only four image systems are plotted. The panels show the  $z = 0.5$  simulation distribution (top-left) dynamically young semi-analytic substructure distribution (top-right), the dynamically old semi-analytic distribution (bottom-right), and the  $z = 0$  simulation distribution (bottom-left).

Given the importance of fixing the center of the potential, an interesting question to ask is how well must the center of the lensing potential be known for astrometric perturbations to be sizeable. We address this question in Figure 7, where we test the residual distributions of lenses with substructure for single point source systems where the center of the potential is constrained with a Gaussian prior. As can be seen from the figure, a Gaussian prior of 5 mas does not result in much improvement relative to the case with no prior (the jet source case), while a prior of 1 mas results in a residual distribution similar to that obtained when we fixed the center of the potential (our fiducial single point source case). Thus, we expect that the center of the potential must be known to  $\approx 1$  mas accuracy for substructure perturbations to be

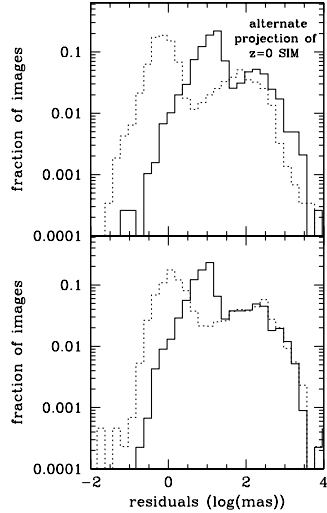


FIG. 8.— Histograms of the residuals between modeled and observed images in milliarcseconds for our alternate projection of the  $z = 0$  simulation substructure model that projects a large sub-clump near the center of the system. Only four image systems are plotted. *Top:* Single point source systems using 7 fitted parameters and fixing the center of the lens potential are plotted in the solid line and jet source systems using 11 fitted parameters are shown in the dotted line. *Bottom:* Histograms of the residuals between modeled and observed images in milliarcseconds for single point source systems using 7 fitted parameters and Gaussian priors on the center of the lens potential of 5 mas (dotted) and 1 mas (solid).

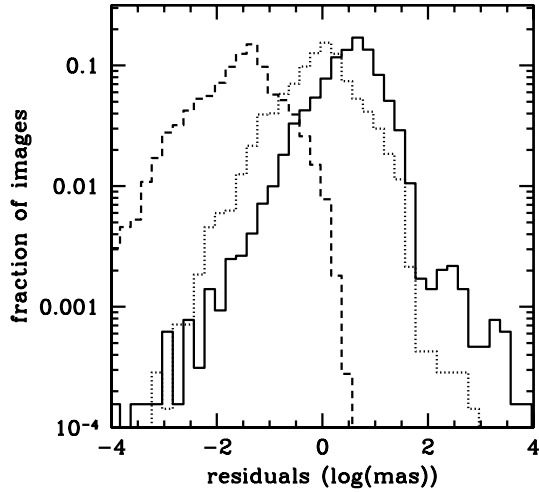


FIG. 9.— Histograms of the residuals between modeled and observed images in milliarcseconds for the dynamically old semi-analytic substructure model. Only four image systems are plotted. Single point source systems using 7 fitted parameters and fixing the center of the lens potential are plotted. The fiducial result is shown by a solid line. Increasing the concentration by 2 (at fixed mass) is shown by a dotted line and increasing the concentration by 10 is shown by a dashed line.

non-degenerate with an allowed shift of the center of the lensing potential. As discussed previously, the results of Yoo et al. (2005) suggest that the assumption that the lensing galaxy represents the center of the lens potential holds to within 5 to 10 mas. Detailed model fits of Hubble Space Telescope (HST) data shows that lens galaxy astrometry down to 2 mas are achievable (e.g.,

Impey et al. 1998; Lehár et al. 2000).

#### 4.3. Massive Substructures Near the Einstein Radius

One additional possibility we consider is what happens when an extremely massive substructure projects near the Einstein radius of the lens. This question is relevant not only because one expects such cases to result in the largest residuals, but also because, observationally, a large fraction of the current lens sample is seen to have luminous satellites projected near the Einstein radius. While luminous satellites can be directly included in the lens model, it is still interesting to ask what residuals would a similar dark substructure produce.

To address this question, we have chosen an alternate projection of the  $z = 0$  simulation model in which the most massive halo substructure gets projected to within  $\sim 2''$  of the halo center. We choose the  $z = 0$  simulation model because this model contains the largest subclump among our four substructure realizations with a mass of about  $\sim 7\%$  of the *host halo* mass. A dark subhalo of this size is unlikely, but it is interesting to test the extremes necessary for large astrometric perturbations.

The resulting residual distributions for this substructure model are shown in Figure 8 for both a single point source (top panel, solid line) and a jet source (top panel, dotted line). The same basic qualitative features as seen in the fiducial cases are found in this projection. The peak residual for the single source case is  $\approx 10$  mas and drops to  $\approx 1$  mas for the jet source case. The total amount of substructure within  $2''$  of the lens center in this projection is significantly larger than those found for the fiducial substructure models, but the peak residuals are only somewhat larger. We also show in the bottom panel the residual distributions obtained using 1 mas (solid) and 5 mas (dotted) Gaussian priors on the center of the lensing potential and using only a single point source. We again find that the center of the lensing potential must be known to within about 1 mas for the position residuals to be sizeable.

#### 4.4. Dependence on the Concentration of Subhalos

In the previous sections, we have preferentially chosen substructure realizations that would maximize the numbers of subhalos projected near the center of the lens – using semi-analytic substructure models and choosing the line-of-sight along the major axis – thereby maximizing the estimated signal from substructure. For distributions with significant numbers of subhalos projected near the Einstein radius, the peak of the residual distribution is a few milliarcseconds. As discussed previously, however, the subhalos in both the simulation-based substructure models and the semi-analytic substructure models could be biased to lower concentrations. Higher concentrations may lead to larger deflections but may require better alignment with images. In Figure 9, the residual distribution for the fiducial dynamically old semi-analytic substructure realization is compared to the same realization where the concentration of each subhalo is doubled while the mass and tidal radius of each subhalo is held fixed and to the realization where the concentration is increased by an order of magnitude. Here, it can be seen that the peak of the residual distribution is *lowered* when the concentration of clumps is increased, so, in fact, our

estimates likely represent the largest values for astrometric perturbations.

#### 4.5. Halo-to-Halo Variation

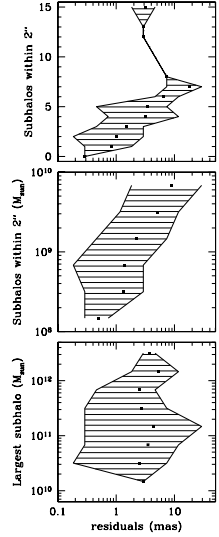


FIG. 10.— The peak of the residual distributions for 4-image single point source lens systems for 48 semi-analytic substructure models using a random line-of-sight. The average residual peak size is shown as square points, enclosed within the minimum and maximum peak residuals values. *Top*: The average peak residual compared to the number of subhalos within 2'' of the halo center. *Center*: The average peak residual compared to the total mass in subhalos within 2'' of the halo center. *Bottom*: The average peak residual compared to the mass of the largest subhalo in each distribution.

The fiducial substructure distributions show that the size of modeled residuals increases with a greater amount of subhalos projected near to image positions. Halo-to-halo variation, however, could swamp this effect. A full statistical analysis of halo-to-halo variation would require a more extensive understanding of both observational biases and substructure model parameters. In this section, we test the possible range of the scatter using 48 different substructure distributions drawn from the semi-analytic models discussed previously and including the two fiducial semi-analytic models. Testing single point source systems with a random line-of-sight, these semi-analytic substructure models have between zero and fifteen subhalos within 2 arcsecs of the center of the halo. Most of the substructure realizations contain between three and five clumps within 2 arcsec of the center of the halo. The number of models with a particular number of nearby clumps cannot be ascribed any particular significance, however, a relationship between the number of nearby clumps and the mean of the peak of the residual distribution may be seen in the top panel of Fig. 10. The range of residuals peaks in the bins is also shown in this figure, where, for the most populated bins, the scatter is significant, but not as large as the total range of peak distributions. For all the models, the residuals fall between 0.1 mas and 30 mas. A similar correlation is found between the average peak residual and the total mass of subclumps within 2 arcsec. For comparison, we also plot the average peak residual compared to the mass of the

largest subhalo. Here, no clear correlation can be observed.

#### 4.6. Discussion

Our results indicate that systems with massive substructures within the area of the Einstein radius result in the largest residuals, of a few mas, which are an order of magnitude larger than residuals for substructure distribution with no nearby clumps. Just as importantly, however, we have found that without milliarcsecond constraints on the center of the lensing potential, astrometric perturbations from substructures are sufficiently degenerate with changes in the position of the lensing potential so as to reduce modeled residuals by an order of magnitude and making the residuals extremely difficult to detect on the basis of astrometric perturbations alone. Yoo et al. (2005) have suggested that the assumption that the lensing galaxy represents the center of the lens potential holds to within 5 to 10 mas. Astrometry of less than a few milliarcseconds for lensed galaxies may be achieved using detailed model fits of Hubble Space Telescope (HST) data (e.g., Impey et al. 1998; Lehár et al. 2000).

Interestingly, Biggs et al. (2004) have presented a four image jet source system, CLASS B0128+437, in which reproducing the observations with a smooth mass model appears to be difficult, even while allowing the center of the lensing potential float. More specifically, the largest position residuals they find are of order a few mas. Such large perturbations are comparable to the highest peak residuals we found, and suggest a large substructure mass fraction at radii near the Einstein radius. The errors in the original Dalal & Kochanek (2002) result are large enough to include both small and large substructure mass fractions (0.6% to 7% within the 90% confidence intervals). In simulations, Mao et al. (2004) found that the substructure mass fraction at radii near the positions is small,  $\sim 0.5\%$  – as small as the amount of substructure found in our projected simulation halos which have small astrometric residuals. In addition, studies of cusp relation anomalies with ray-tracing of simulations of galactic halos with substructure have implied that there is not enough substructure in simulations to account for the observed level of cusp anomalies (Bradač et al. 2004; Amara et al. 2006; Macciò et al. 2006).

Yoo et al. (2005) measured the displacement between the observed position of various lensing galaxies and the position of the best fit lensing model. Their finding of displacements between the two of order 5 to 10 mas imply that the center of the lens potential and the position of the lensing galaxy are at least roughly coincident, but they also suggest that the displacements may indicate an alternative way to measure the substructure mass fraction. Displacements of this size are consistent with the typical displacements we observed, modeling our clumpy lenses with smooth macromodels. However, when we allowed the center of the potential to float using jet sources, we found that that even when there were no substructures or an extremely small substructure mass fraction within 2'' of the center of the lens, the center of the potential was still displaced by a few to tens of milliarcseconds. This suggests that such displacements are sensitive to substructure far from the Einstein radius of the lens, and hence interpretation of such observations

as limits on the substructure mass fraction in the central regions of lenses might be subject to some caveats. Further investigation of whether the substructure mass fraction can be robustly estimated from mis-alignment of the observed position of the lensing galaxy with the best fit location for the center of the potential is clearly warranted.

## 5. DETECTING SUBSTRUCTURE IN JET SYSTEMS

Given the difficulties in using lens modeling to probe substructure distributions, unambiguous detections of substructure in individual lenses might be more robustly achieved through local measures of astrometric perturbations. By offering more observational constraints, jet source systems seem particularly promising avenue of research.

### 5.1. Astrometric Signatures of Substructure

Given a perfectly straight jet source small enough that lensing can be locally linearized, its images will also be perfectly straight. If one were to observe a lensed jet with two images, one straight and one with a kink, one might be tempted to conclude that the kink must have been introduced by a local small scale perturbation to the lensing potential. However, large kinks may also arise in the absence of substructures since small deviations from linearity in the jet can be greatly amplified when the lens mapping is nearly singular.<sup>6</sup> In general, then, without *a priori* knowledge of the linearity of a jet source, some degree of modeling is required to detect substructure.

### 5.2. Local Lens Modeling

In this subsection we consider one possible method for detecting astrometric perturbations using purely local information from the images (i.e., eschewing global lens modeling). We consider lensed images of sources where multiple source subcomponents are resolved and where each of the subcomponents is multiply imaged. Moreover, we assume the images are in a fold configuration, and focus our attention on the close pair of images. Assuming the size of the source is smaller than any length scale associated with the lensing potential, the mapping between the source and each of its images may be linearized. Letting  $A_+$  and  $A_-$  denote the inverse magnification tensors describing the mapping from the positive and negative parity images, respectively, onto the source, the two images must themselves be related via a linear transformation,  $\delta\mathbf{x}_+ = U \cdot \delta\mathbf{x}_-$ , where  $U = (A_+)^{-1} A_-$  and  $\delta\mathbf{x}_\pm$  denotes the image position vectors in any coordinate system chosen such that the origins in the lens plane maps to a single origin point in the source plane. Moreover, the assumption that the images are in a fold configuration puts a constraint on the form of the matrix  $U$ , so deviations on the form of the matrix  $U$  from its expected structure may signal the presence of substructures on scales comparable to or smaller than the

<sup>6</sup> While bent radio jets do not, in general, imply the presence of substructure, some lens configurations can be described that would unambiguously signal the presence of localized perturbations. For instance, if two jets in a fold configuration – where two of four lensed images are close together – are bent in the same sense, one would associate the same parity to both images, violating a generic prediction of smooth lensing potentials.

separation between images. The goal of this section is to investigate this possibility quantitatively.

Operationally, we proceed as follows. Given a jet with three subimages, we define the best-fit linear transformation  $U$  by minimizing the total residual  $\langle \Delta r \rangle$  defined by

$$\langle \Delta r \rangle = \sqrt{\frac{1}{N} \left( \sum_{i=1}^N \left| (\mathbf{x}_+^{(i)} - \mathbf{x}_+^{(0)}) - U \cdot (\mathbf{x}_-^{(i)} - \mathbf{x}_-^{(0)}) \right|^2 \right)}, \quad (5)$$

where the sum is over the position vectors,  $\mathbf{x}_\pm^{(i)}$  is the image position of vector  $i$ ,  $\mathbf{x}_\pm^{(0)}$  is the image position chosen as the origin of the coordinate system, and  $N$  is the number of terms in the sum. For three jet subcomponents,  $N = 2$ , so fitting is overconstrained if the matrix  $U$  has three free parameters or less. Here, we constrain the form of the relative distortion matrix  $U$  using the well known fact that for smooth lenses fold images are expected to have equal and opposite magnifications as the image separation goes to zero. We thus set the condition  $\det(U) = -1$ ; violations of this condition may be indicative of substructure. It is worth noting that this constraint is coordinate independent, so fitting can be done in any appropriate, observationally-defined coordinate system without any loss of generality. For completeness, appendix A explicitly performs a Taylor series expansion of the lensing potential around a specific point along the lens's critical curve and in a specific coordinate system, though we found this more detailed analysis to be less sensitive to substructure than the simpler approach presented here.

The properties of the distribution of the residual  $\Delta r$  also depend on the assumed properties of the jet source. The magnitude of the residual scales with distance between jet subcomponents, which we take to be 1 mas in our examples. More interestingly, we will find that the distribution of  $\Delta r$  depends on the *jet bending angle*, the angle between the two relative position vectors of the source subcomponents. Thus, a zero degree bending angle corresponds to a perfectly straight jet.

Figure 11 shows the  $\langle \Delta r \rangle$  distribution while enforcing  $\det(U) = -1$  for various jet bending angles. Solid lines are obtained in the no substructure case, and the cross-hatched histograms correspond to the case of the dynamically old semi-analytic substructure model. We can see that for straight or nearly straight jets, the substructure and no substructure cases are indistinguishable. As the jet becomes non-linear (the bending angle increases), the  $\Delta r$  distributions for the substructure case starts to extend to higher  $\Delta r$  values, implying that nonlinear jets may in principle detect substructure through this local test, but only if the substructure density is high enough. Indeed, the simulation substructure models are always indistinguishable from the no substructure case, which is not unexpected given the lack of substructures in the central regions of the halo.

Our result in Figure 11 might seem surprising: linear jets are ineffective at detecting substructure without the full lens modeling. As suggested strongly by section §4, the simple picture of substructure producing a bend in a single image while leaving the other untouched seems overly naive. Moreover, jets that are bent to begin with

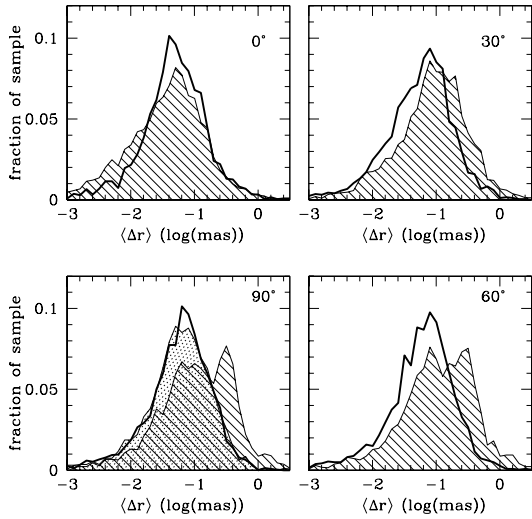


FIG. 11.— Distribution of  $\langle \Delta r \rangle$  for different jet bending angles. Clockwise from top-left, the bending angles are 0, 30, 60, and 90 degrees. The thick solid line shows the distribution for the smooth, no substructure model, while the cross-hatched region shows the distribution for the old, semi-analytic substructure model in the 0, 30, 60 degree panels and increasing in deviation from the no substructure case. In the 90 degree panel, an additional shaded, dotted region shows the distribution for the  $z = 0$  simulation substructure model, which does not appreciably deviate from the no substructure case.

can detect substructure. We interpret the bending angle dependence as follows: for a perfectly linear jet, observations of the jet constrain the lensing distortion along the single jet axis only, so the correct amount of distortion can be reproduced in the substructure realizations regardless of the  $\det(U) = -1$  constraint. For bent jets, however, the distortion along two different axis is probed, so *both* eigenvalues of the relative distortion matrix can be constrained by observations. Since the  $\det(U) = -1$  condition specifies a relation between these two eigenvalues, it is not surprising that only when both eigenvalues are resolved can the effects of substructures be discerned.

## 6. LUMINOUS SATELLITES

In the previous sections, we have focused on cases where the substructure producing astrometric perturbations is dark. However, luminous satellites can perturb image positions as well, and in a number of strong lensing systems, bright satellites have been detected near the lensed images. Such systems are important for several reasons. First, and most obviously, much more can be learned about the subhalo if its position is known: since the astrometric perturbation  $\delta\alpha \propto m/r$  for a satellite of mass  $m$  and distance  $r$ , a given perturbation can be produced by a nearby low-mass subhalo or a distant high-mass subhalo. Additionally, by comparing the lensing properties of luminous satellites to those of dark subhalos, we can address why some subhalos are dark and some are luminous. Gravitational lensing can help resolve this question by directly measuring the masses associated with satellites falling near lensed images. We illustrate this by considering two systems, MG J0414+0534 (Trotter et al. 2000; Ros et al. 2000) and MG J2016+112 (Koopmans et al. 2002), which both have lenses at redshift  $z \sim 1$ . A key advantage of

these systems over other lenses with known satellites (e.g. RXJ0911+0551) is that both have been observed with high-resolution VLBI imaging, giving astrometry at the sub-milliarcsecond level. We infer the satellite masses in these systems by modeling the lensed image positions only, ignoring the image fluxes. We hold fixed the position of the main lens galaxy and the satellite at the observed locations relative to the images, and model the mass distribution using a singular isothermal ellipsoid for the main lens and singular isothermal sphere for the satellite, also allowing for arbitrary external shear. We run a grid of models for many values of the velocity dispersion of the satellite, optimizing over all other parameters, and define the likelihood as  $L = \exp(-\chi^2/2)$ . For MG J0414+0534, astrometric data and uncertainties were taken from Trotter et al. (2000), while for MG J2016+112 these were taken from Koopmans et al. (2002). The satellite in MG J0414+0534, referred to as Object X, has apparent magnitude  $R = 24.6$  corresponding to absolute magnitude of -19.4 for a  $\Lambda$ CDM cosmology with  $\Omega_M = 0.27$  and  $h = 0.71$ . The satellite G1 in MG J2016+112 has  $I = 24.6$ , corresponding to an absolute magnitude of -19.6.

The results of this procedure are plotted in Figure 12. For MG J0414+0534, the velocity dispersion  $\sigma$  of the satellite Object X was found to be  $81 < \sigma < 102$  km/s at 95% confidence. For MG J2016+112, satellite G1 was found to have velocity dispersion  $87 < \sigma < 101$  km/s at 95% confidence. Note that these correspond to quite large masses. For comparison, the Milky Way Galaxy's largest satellite, the LMC, has an equivalent velocity dispersion  $\sigma \approx v_{\text{rot}}/\sqrt{2} \approx 50$  km s $^{-1}$  and a  $V$ -band integrated magnitude of  $\sim -18$ . While the satellites in these systems are apparently rather massive, note that the lensing constraints were of sufficient quality to detect masses nearly an order of magnitude smaller.

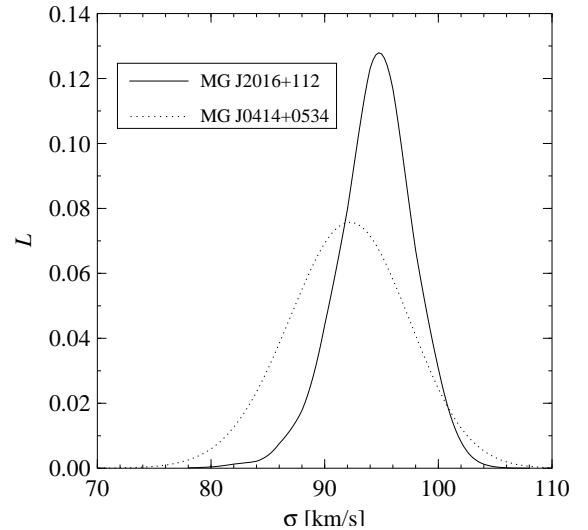


FIG. 12.— Lensing constraints on satellite masses. The solid and dashed curves, respectively, show likelihood as a function of velocity dispersion  $\sigma$  for the satellites in lens systems MG J2016+112 and MG J0414+0534, where the satellite mass distribution is modeled as a singular isothermal sphere.

## 7. SUMMARY AND CONCLUSIONS

Astrometric perturbations from substructure lensing offers a new avenue for probing distributions of DM substructure in galactic halos. Previous work in this field has mostly probed the effects of single perturbers on image positions (Metcalf & Madau 2001; Inoue & Chiba 2003, 2005a,b), though Chiba (2002) investigated the lens system B1422+231 using a simple model in which CDM substructures were modeled as point masses – finding that typical astrometric perturbations are of order 10 to 20 mas. Since, observations of the strong lens system B0128+437 with submilliarcsecond resolution have found astrometric residuals to the best fit models to be slightly smaller at roughly 5 to 10 mas. Such residuals, however, are large enough to be significant relative to measurement errors (Biggs et al. 2004). In light of these finding, the question of how large astrometric perturbations by CDM substructures are is a very timely one.

In this paper, we use realistic models of substructure in order to create populations of artificial lens and estimate the residuals between modeled and observed image positions. Substructure distributions were drawn from DM simulations and semi-analytic models in order to bracket the expected abundance of dark matter substructures in the inner regions of galaxy size halos. Our results can be summarized as follows:

1. In general, astrometric perturbations from substructure are partly degenerate with the smooth macromodel. Intrinsic image position perturbations from substructure are typically of order  $\gtrsim 10$  mas, even when few to no substructures are projected near the center of the lens. Modeled residuals are significantly smaller by about an order of magnitude.
2. Substructure distributions in which clumps project near the Einstein radius of the lens appear to be the least degenerate with the macromodel parameters and, therefore, cause the largest residuals between the observed and modeled image positions. When the center of the lens potential is fixed, substructure models with significant amounts substructure projected near the Einstein radius have modeled residuals of order a few milliarcseconds.
3. Substructure astrometric perturbations appear to be coherent on scales comparable to the extent of typical radio jets. This coherence significantly enhances the degree to which substructure perturbations are degenerate with a change in the center of the lensing potential. Allowing the center of the potential to be fit as a parameter results in modeled residuals that are an order of magnitude smaller than would be the case if submilliarcsecond constraints of the center of the lensing potential were obtained.
4. Tests of additional substructure realizations suggest that  $\sim 10$  mas may represent the largest residuals

for any realistic substructure distributions where the center of the lens potential is fixed. These substructure realizations include nearby, massive dark subhalos and more concentrated halos.

5. Local lens modeling of jet sources can in principle detect substructure perturbations provided there exist substructures within the Einstein radius of the lens in consideration and the jet sources are intrinsically bent.
6. Using gravitational lensing, it is possible to place constraints on the masses of luminous substructures of observed gravitational lenses through detailed lens modeling. These constraints may be used to test proposed mechanisms for star formation in DM subhalos.

This work suggests that lens modeling may provide an avenue for detecting substructure through astrometric perturbations. Substructure distributions which project subclumps near the Einstein radius of the lens halo cause the greatest perturbations; however, substructure catalogs from simulations and semi-analytic models suggest that the scale of the perturbations will be small, on the order of a few milliarcsecond. However, unlike anomalous flux ratios between lensed images which have been thoroughly investigated in previous works (e.g., Mao & Schneider 1998; Metcalf & Madau 2001; Dalal & Kochanek 2002; Kochanek & Dalal 2004; Rozo et al. 2006), a complete accounting of the effects of astrometric perturbations and their observational implications has not yet been done; for example, observational biases remain unexplored. The results of future studies will offer a better understanding of submilliarcsecond resolution observations of strong lens systems.

This research was carried out at the University of Chicago, Kavli Institute for Cosmological Physics and was supported (in part) by grant NSF PHY-0114422. KICP is a NSF Physics Frontier Center. J.C. was supported by the National Science Foundation (NSF) under grants No. AST-0206216 and AST-0239759, and by NASA through grant NAG5-13274. Cosmological simulations used in this analysis were performed on the IBM RS/6000 SP4 system (**copper**) at the National Center for Supercomputing Applications (NCSA).

We are grateful to Stefan Gottlöber and Anatoly Klypin for providing us the high-resolution cluster simulation used in this study.

J.E.T was supported by the Leverhulme Trust, the U.K. Particle Physics and Astronomy Research Council (PPARC), the NSF under grant AST-0307859, and the DoE under contract DE-FG02-04ER41316.

J.C. acknowledges the hospitality of the IAS, where part of this work was done. E.R. thanks David Rusin for helpful discussions related to this work.

## REFERENCES

Amara, A., Metcalf, R. B., Cox, T. J., & Ostriker, J. P. 2006, MNRAS, 367, 1367

Benson, A. J., Lacey, C. G., Baugh, C. M., Cole, S., & Frenk, C. S. 2002, MNRAS, 333, 156

Benson, A. J., Lacey, C. G., Frenk, C. S., Baugh, C. M., & Cole, S. 2004, MNRAS, 351, 1215

Biggs, A. D., Browne, I. W. A., Jackson, N. J., York, T., Norbury, M. A., McKean, J. P., & Phillips, P. M. 2004, MNRAS, 350, 949

Bradač, M., Schneider, P., Lombardi, M., Steinmetz, M., Koopmans, L. V. E., & Navarro, J. F. 2004, A&A, 423, 797

Bradač, M., Schneider, P., Steinmetz, M., Lombardi, M., King, L. J., & Porcas, R. 2002, A&A, 388, 373

Bullock, J. S., Kolatt, T. S., Sigad, Y., Somerville, R. S., Kravtsov, A. V., Klypin, A. A., Primack, J. R., & Dekel, A. 2001, MNRAS, 321, 559

Bullock, J. S., Kravtsov, A. V., & Weinberg, D. H. 2000, ApJ, 539, 517

Chiba, M. 2002, ApJ, 565, 17

Dalal, N., & Kochanek, C. S. 2002, ApJ, 572, 25

Diemand, J., Moore, B., & Stadel, J. 2004, MNRAS, 352, 535

Gao, L., White, S. D. M., Jenkins, A., Stoehr, F., & Springel, V. 2004, MNRAS, 355, 819

Ghigna, S., Moore, B., Governato, F., Lake, G., Quinn, T., & Stadel, J. 2000, ApJ, 544, 616

Hannestad, S., & Scherrer, R. J. 2000, Phys. Rev. D, 62, 43522

Hayashi, E., Navarro, J. F., Taylor, J. E., Stadel, J., & Quinn, T. 2003, ApJ, 584, 541

Hu, W., Barkana, R., & Gruzinov, A. 2000, Phys. Rev. Lett., 85, 1158

Impey, C. D., Falco, E. E., Kochanek, C. S., Lehár, J., McLeod, B. A., Rix, H.-W., Peng, C. Y., & Keeton, C. R. 1998, ApJ, 509, 551

Inoue, K. T., & Chiba, M. 2003, ApJ, 591, L83

—. 2005a, ApJ, 634, 77

—. 2005b, ApJ, 633, 23

Kazantzidis, S., Mayer, L., Mastropietro, C., Diemand, J., Stadel, J., & Moore, B. 2004, ApJ, 608, 663

Keeton, C. R., & Zabludoff, A. I. 2004, ApJ, 612, 660

Klypin, A., Gottlöber, S., Kravtsov, A. V., & Khokhlov, A. M. 1999a, ApJ, 516, 530

Klypin, A., Kravtsov, A. V., Valenzuela, O., & Prada, F. 1999b, ApJ, 522, 82

Kochanek, C. S., & Dalal, N. 2004, ApJ, 610, 69

Koopmans, L. V. E., Garrett, M. A., Blandford, R. D., Lawrence, C. R., Patnaik, A. R., & Porcas, R. W. 2002, MNRAS, 334, 39

Kravtsov, A. V. 1999, Ph.D. Thesis

Kravtsov, A. V., Berlind, A. A., Wechsler, R. H., Klypin, A. A., Gottlöber, S., Allgood, B., & Primack, J. R. 2004a, ApJ, 609, 35

Kravtsov, A. V., Gnedin, O. Y., & Klypin, A. A. 2004b, ApJ, 609, 482

Kravtsov, A. V., Klypin, A. A., & Khokhlov, A. M. 1997, ApJS, 111, 73

Lehár, J., Falco, E. E., Kochanek, C. S., McLeod, B. A., Muñoz, J. A., Impey, C. D., Rix, H.-W., Keeton, C. R., & Peng, C. Y. 2000, ApJ, 536, 584

Macciò, A. V., Moore, B., Stadel, J., & Diemand, J. 2006, MNRAS, 366, 1529

Mao, S., Jing, Y., Ostriker, J. P., & Weller, J. 2004, ApJ, 604, L5

Mao, S., & Schneider, P. 1998, MNRAS, 295, 587

Mayer, L., Moore, B., Quinn, T., Governato, F., & Stadel, J. 2002, MNRAS, 336, 119

Metcalf, R. B. 2002, ApJ, 580, 696

Metcalf, R. B., & Madau, P. 2001, ApJ, 563, 9

Moore, B., Ghigna, S., Governato, F., Lake, G., Quinn, T., Stadel, J., & Tozzi, P. 1999, ApJ, 524, L19

Moore, B., Katz, N., & Lake, G. 1996, ApJ, 457, 455

Morgan, N. D., Kochanek, C. S., Falco, E. E., & Dai, X. 2006, ApJ, submitted (astro-ph/0605321)

Nagai, D., & Kravtsov, A. V. 2005, ApJ, 618, 557

Pen, U.-L., & Mao, S. 2005, (astro-ph/0506053)

Ros, E., Guirado, J. C., Marcaide, J. M., Pérez-Torres, M. A., Falco, E. E., Muñoz, J. A., Alberdi, A., & Lara, L. 2000, A&A, 362, 845

Rozo, E., Zentner, A. R., Bertone, G., & Chen, J. 2006, ApJ, 639, 573

Schneider, P., Ehlers, J., & Falco, E. E. 1992, Gravitational Lenses (Gravitational Lenses, XIV, 560 pp. 112 figs. Springer-Verlag Berlin Heidelberg New York. Also Astronomy and Astrophysics Library)

Somerville, R. S. 2002, ApJ, 572, L23

Spergel, D. N., & Steinhardt, P. J. 2000, Phys. Rev. Lett., 84, 3760

Stoehr, F. 2002, private communication

Stoehr, F., White, S. D. M., Springel, V., Tormen, G., & Yoshida, N. 2003, MNRAS, 345, 1313

Stoehr, F., White, S. D. M., Tormen, G., & Springel, V. 2002, MNRAS, 335, L84

Tasitsiomi, A., Kravtsov, A. V., Gottlöber, S., & Klypin, A. A. 2004, ApJ, 607, 125

Taylor, J. E., & Babul, A. 2001, ApJ, 559, 716

—. 2004, MNRAS, 348, 811

—. 2005, MNRAS, 364, 535

Toth, G., & Ostriker, J. P. 1992, ApJ, 389, 5

Trotter, C. S., Winn, J. N., & Hewitt, J. N. 2000, ApJ, 535, 671

Wilkinson, M. I., Kleyna, J. T., Evans, N. W., Gilmore, G. F., Irwin, M. J., & Grebel, E. K. 2004, ApJ, 611, L21

Yoo, J., Kochanek, C. S., Falco, E. E., & McLeod, B. A. 2005, ApJ submitted (astro-ph/0511001)

Zentner, A. R., Berlind, A. A., Bullock, J. S., Kravtsov, A. V., & Wechsler, R. H. 2005a, ApJ, 624, 505

Zentner, A. R., Kravtsov, A. V., Gnedin, O. Y., & Klypin, A. A. 2005b, ApJ, 629, 219

## APPENDIX

### TAYLOR SERIES EXPRESSION FOR THE RELATIVE DISTORTION MATRICES OF FOLDS

In this appendix we present a brief derivation of the relative distortion matrix  $U$  for fold images. We use the notation of Schneider et al. (1992) throughout. Let then  $\mathbf{x}$  and  $\mathbf{y}$  represent position vectors on the lens and source plane respectively, and let  $\mathbf{y}_0$  be the point along the lens's caustic that is closest to the source position  $\mathbf{u}$  of interest. We choose the point  $\mathbf{y}_0$  as the origin of the source plane, and its image on the lens plane  $\mathbf{x}_0$  as the origin of the lens plane. Moreover, we choose our axis so that the inverse magnification tensor  $A$  at  $\mathbf{x}_0$  is diagonal, with the  $(1, 1)$  component non-zero.

With these assumptions, Schneider et al. (1992, equation 6.16) show that one one possible parametrization  $\mathbf{y}_c(\lambda)$  of the lens's caustic around  $\mathbf{y}_0$  is given by

$$\mathbf{y}_c(\lambda) = \left( \begin{array}{c} \lambda \\ \frac{bd-c^2}{2a^2d} \lambda^2 \end{array} \right). \quad (\text{A1})$$

Note that  $\lambda = 0$  corresponds to  $\mathbf{y} = 0$ , that is the source plane origin. Given the source position of interest  $\mathbf{u}$ , and using the fact that, by definition, its distance to the caustic  $d^2(\lambda) = |\mathbf{u} - \mathbf{y}_c(\lambda)|^2$  is minimized at the origin, we obtain the constraint equation

$$0 = \left( \frac{d}{d\lambda} |\mathbf{u} - \mathbf{y}_c(\lambda)|^2 \right) \Big|_{\lambda=0} \quad (\text{A2})$$

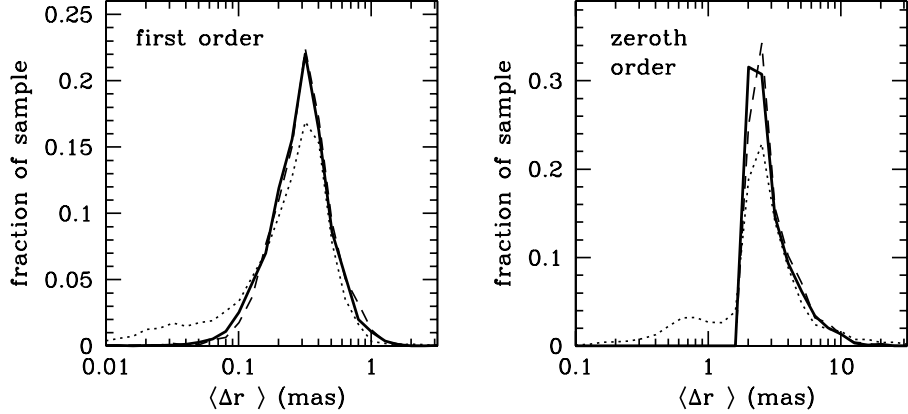


FIG. 13.— The  $\langle \Delta r \rangle$  (mas) distribution for a sample of realizations of fold image configurations with a 90 degree jet bending angle. The thick, solid line represents the no substructure case. The dotted line indicates the dynamically old semi-analytic substructure distribution and the dashed line corresponds to the  $z = 0$  simulation substructure catalog. *Left:* The first order expansion for  $U$ , Eqn. A6, is tested. *Right:* The zeroth order expansion, Eqn. A10, is tested.

which simplifies to  $u_1 = 0$ . In other words, the coordinate system we have chosen has the property that the source position of interest  $\mathbf{u}$  falls exactly along the  $y$  axis. Consequently, from now on we assume  $\mathbf{u} = (0, u)$ .

Given this source position, its corresponding images  $\mathbf{x}_+$  and  $\mathbf{x}_-$  in the lens plane are given by (see Schneider et al. (1992) equation 6.17)

$$(\mathbf{x}_\pm)_1 = -\frac{cu}{ad} \quad (A3)$$

$$(\mathbf{x}_\pm)_2 = \pm \sqrt{\frac{2u}{d}} \quad (A4)$$

where we have defined the Taylor series coefficients  $a = \phi_{11}^{(0)}$ ,  $b = \phi_{112}^{(0)}$ ,  $c = \phi_{122}^{(0)}$ , and  $d = \phi_{222}^{(0)}$ . It is important to emphasize that the above results implies that in the coordinate system we have chosen, the image separation vector for fold images is along the  $y$  axis. Moreover, since the  $x$  axis is simply orthogonal to the  $y$  axis, *the coordinate system chosen for the expansion can be observationally determined* up to an overall displacement of the origin.

Returning to our derivation, in terms of the expansion coefficients, the inverse magnification tensor  $A(\mathbf{x})$  at an arbitrary lens plane position  $\mathbf{x}$  near the fold is given by (Schneider et al. 1992, equation 6.14)

$$A(\mathbf{x}) = \begin{pmatrix} a + bx_2 & bx_1 + cx_2 \\ bx_1 + cx_2 & cx_1 + dx_2 \end{pmatrix}, \quad (A5)$$

so that the relative distortion matrix between the two images of interest is given by  $U = (A_+)^{-1} A_-$  where  $A_\pm = A(\mathbf{x}_\pm)$ . To lowest order in  $u$ , we find

$$U = \begin{pmatrix} 1 + (\epsilon_1 + \epsilon_2) & 0 \\ -k(1 + \epsilon_2) & -1 + (\epsilon_1 - \epsilon_2) \end{pmatrix} \quad (A6)$$

where we have defined the quantities

$$k = \frac{2c}{d} \quad (A7)$$

$$\epsilon_1 = \frac{c^2 - 2bd}{\sqrt{2ad^{3/2}}} u^{1/2} \quad (A8)$$

$$\epsilon_2 = \frac{3c^2 - 2bd}{\sqrt{2ad^{3/2}}} u^{1/2}. \quad (A9)$$

Note that the inverse of this matrix is obtained by simply reversing the signs of  $\epsilon_1$  and  $\epsilon_2$ . The relative distortion matrix in the limit  $u \rightarrow 0$  is simply given by

$$U = \begin{pmatrix} 1 & 0 \\ -k & -1 \end{pmatrix}. \quad (A10)$$

which has a single free parameter to be determined, and  $\det(U) = -1$  as it should.

Figure 13 shows the distribution of the average residual  $\langle \Delta r \rangle$  given by equation 5 using the zeroth order and first order expansions of the matrix  $U$  computed above, using the same fold configurations as in Figure 11 for a jet bending angle of 90 degrees. The coordinate system chosen for the expansion is approximated by setting the  $y$  axis in the image

plane to be in the direction of the vector between the fold images. As can be seen from the figure, the substructure and no substructure residual distributions are indistinguishable.

It is intriguing that a careful expansion of the lensing potential resulted in a test that is *less* sensitive to substructures than the more simple minded approach taken in the main body of this work. It is possible that this difference simply reflects the fact that the expectation  $\det(U) = -1$  is generic, and not particular to a specific point about which the potential is expanded. Since the form of the matrix  $U$  explicitly depends on the point along about which the lensing potential is expanded, it is possible that a formal expansion about a different origin from the one considered here would result in a test of higher sensitivity to substructures.